LM-01K133
March 20, 2001

Zinc Treatment Effects on Corrosion Behavior of 304 Stainless Steel in High Temperature, Hydrogenated Water

S.E. Ziemniak, M. Hanson

Zinc Treatment Effects on Corrosion Behavior of 304 Stainless Steel in High Temperature, Hydrogenated Water

S. E. Ziemniak *
M. Hanson

Lockheed Martin Corporation
P.O. Box 1072
Schenectady, New York 12301-1072

* Corresponding author. Tel.: +1-518-395-6887; fax: +1-518-395-7298.
E-mail address: ziemnia@kapl.gov

ABSTRACT

Trace levels of soluble zinc(II) ions (30 ppb) maintained in mildly alkaline, hydrogenated water at 260°C were found to lower the corrosion rate of austenitic stainless steel (UNS S30400) by about a factor of five, relative to a non-zinc baseline test [3] after 10,000 hr. Characterizations of the corrosion oxide layer via grazing incidence X-ray diffraction and X-ray photoelectron spectroscopy in combination with argon ion milling and target factor analysis, confirmed the presence of two spinel oxide phases and minor amounts of recrystallized nickel. Based on the distribution of the three oxidized alloying constituents (Fe, Cr, Ni) with respect to depth and oxidation state, it was concluded that: (a) corrosion occurs in a non-selective manner, but approximately 30% of the oxidized iron is released to the water, and (b) the two spinel oxides exist as a ferrite-based outer layer $(Ni_{0.1}Zn_{0.6}Fe_{0.3})(Fe_{0.95}Cr_{0.05})_2O_4$ on top of a chromite-based inner layer $(Ni_{0.1}Zn_{0.2}Fe_{0.7})(Fe_{0.4}Cr_{0.6})_2O_4$. These results suggest that immiscibility in the Fe_3O_4-$ZnFe_2O_4$ binary may play a role in controlling the zinc content of the outer layer. On the other hand, the lower corrosion rate caused by zinc additions is believed to be a consequence of corrosion oxide film stabilization due to the substitution reaction equilibrium:

$$z\ Zn^{2+}(aq) + FeCr_2O_4(s) \rightleftharpoons z\ Fe^{2+}(aq) + (Zn_zFe_{1-z})Cr_2O_4(s)$$

The liquid-solid distribution coefficient for the reaction, defined by the ratio of total zinc to iron ion concentrations in solution divided by the Zn(II)/Fe(II) ratio in the solid, z/(1-z), was found to be 0.184. This interpretation is consistent with the benefits of zinc treatment being concentration dependent.

KEYWORDS: (A) stainless steel, sputtered films; (B) XPS, AES; (C) oxidation

INTRODUCTION

The development of austenitic stainless steels was one of the most significant metallurgical accomplishments of the Twentieth Century. The German word *rostfrei* was, in fact, used by the inventor of this material because the alloy was considered to be ...'absolutely rustproof in damp air' [1]. Subsequent high temperature application to nuclear reactor coolant systems has revealed that austenitic stainless steels corrode at small, but finite, rates. Furthermore, the transport and activation of stainless steel corrosion products has led to the development of Zn(II) ion additions to the coolant of light water reactors as a method to further minimize the consequences of stainless steel corrosion [2].

The outstanding passivity of austenitic stainless steels to a variety of oxidants is associated with the formation of a protective chromite-based oxide, MCr_2O_4. Recently, we characterized the corrosion film formed on 304 stainless steel in hydrogenated water at elevated temperature [3] and found the inner layer to consist of the solid solution $(Ni_{0.2}Fe_{0.8})(Cr_{0.7}Fe_{0.3})_2O_4$. The important point is that this chromite compound is a spinel: its metal cations are located at interstitial sites in the oxygen lattice having two kinds of symmetry – octahedral and tetrahedral. Because the Cr(III) cation has a strong preference for octahedral sites [4], its spinel oxides are observed to be normal spinels in which the divalent metal cations are contained in tetrahedral sites. It follows that the Zn(II) cation, which exhibits a strong tetrahedral site preference [5], will form a $ZnCr_2O_4$ spinel compound that is particularly stable. If no other changes occur, the increased thermodynamic stability of a corrosion oxide, as manifested by a more compact lattice parameter, is expected to provide an increased resistance to oxygen diffusion, cf [6], and thereby lower corrosion rates.

The purpose of this work is to quantify the effects of trace levels of zinc(II) additions (30 ppb) to a mildly alkaline, hydrogenated water on 304 stainless steel by: (1) lowering the corrosion rate and (2) modifying the corrosion oxide layer.

EXPERIMENTAL

Corrosion specimens of type 304 stainless steel (UNS S30400) were exposed at 260°C in a flowing autoclave facility (10 $cm^3 min^{-1}$) comprised of a one-liter, type 347 stainless steel (UNS S34700) vessel, and fed from stainless steel tanks containing deionized, hydrogen-sparged water. The dissolved hydrogen concentration was 45 scm^3/kg water; alkalinity was buffered to maintain pH (@260°C) = 6.70. A packed bed of granular zinc(II) oxide, located upstream of the test autoclave, was used to supply constant, trace levels of soluble zinc(II) ions. Target zinc concentrations (~30 ppb) were achieved by controlling the feedwater temperature, since the solubility behavior of ZnO had been previously determined as a function of temperature [7]. Test shutdowns, along with specimen removals and insertions, occurred intermittently, so that exposure times ranged between 1000 and 10,000 hours.

In anticipation of the precision corrosion film analyses to be performed, one side of each corrosion specimen (5/8″ x 3/4″ x 1/16″) was highly polished (<6 μin AA) using diamond grit paste. Larger, machined coupons (4″ x 3/4″ x .032″) were also prepared and exposed along with the polished specimens. The larger surface area of the former permitted the total quantity of oxidized base metal to be accurately determined via the application of standard chemical descale (i.e., gravimetric) methodology.

ANALYTICAL PROCEDURES

After completion of the test exposure period, the corrosion specimens were subjected to three types of analyses to characterize the states of their oxidized surfaces: (a) scanning electron microscopy (SEM) with X-ray spectroscopy (EDX) , (b) grazing incidence X-ray diffraction (XRD) and (c) X-ray photoelectron spectroscopy (XPS). Due to the unique features of the XRD and XPS analyses, these methodologies are discussed below.

Grazing Incidence X-Ray Diffraction (GIXRD)

Approximate thickness and unit cell dimensions of solid phases in the corrosion oxide layer were determined by GIXRD. Because total oxide thicknesses were <1 μm, the analysis was performed at Brookhaven National Laboratory using Beamline X3B1 of the National Syncrotron Light Source. This station is equipped with parallel beam optics and was operated at an incident X-ray wavelength of 1.14965 Å to reduce sample absorption and minimize the fluorescence background. These conditions are ideal for high resolution analysis of thin film samples that cannot be adequately measured by conventional X-ray sources. The wavelength as well as the detector zero position, was calibrated using a NIST Al_2O_3 standard. The angle of incidence, ϕ, was varied between 0.1 and 1.0° in increments of 0.1°. Spectra were collected at 2θ values between 20 and 68°. Counting time varied between one and two sec, and the step size was always 0.02°.

For X-rays incident on a solid from air, a critical angle (ϕ_c, rad) is known to exist [8], below which total external reflection occurs:

$$\phi_c = (2\delta)^{1/2}$$

where

$$\delta = N_o\left(e^2 / 2\pi mc^2\right)\left(Z\rho / A\right)\lambda^2 = 2.797x10^6(Z\rho / A)\,\lambda^2$$

and Z is the average atomic number, A is the average atomic mass, ρ is the mass density (g/cm^3) and λ is the X-ray wavelength (Å). Substituting Z, A and ρ values for typical spinel oxides (i.e., $NiCr_2O_4$, $NiFe_2O_4$ and $FeCr_2O_4$) into the above yields an expected critical incidence angle $\phi_c = 0.25°$.

The actual relationship between ϕ and penetration depth (D), however, is non-linear and increases rapidly with ϕ in the vicinity of ϕ_c, as the source of diffracted X-rays changes from reflection to absorption [8, 9]:

$$D = \left(\frac{\lambda\sqrt{2}}{4\pi}\right)\left[\sqrt{\left(\phi^2 - \phi_c^{\,2}\right)^2 + 4\left(\delta_i\right)^2} + \phi_c^2 - \phi^2\right]^{-1/2}$$

where $\delta_i = \lambda\mu/(4\pi)$ and μ is the linear absorption coefficient. The corresponding penetration depth at ϕ_c is given by

$$D_c = \left(\frac{\lambda}{4\pi\mu}\right)^{1/2}$$

Given a λ value of 1.150 Å, application of the Bragg-Pierce law [10] gives $\mu = 442.9$ cm^{-1} ($FeCr_2O_4$) and $\mu = 521.1$ cm^{-1} ($NiFe_2O_4$), which allows D_c values to be established as 130-145 Å. An increase in ϕ from 0.2° to 0.3° increases the 'sampling' depth from about 40 to 700 Å.

X-Ray Photoelectron Spectroscopy (XPS)

The composition (elemental and oxidation state) of each corrosion specimen was investigated as a function of depth by successively removing surface material by argon bombardment and analyzing the

freshly uncovered surface by XPS. This analysis was performed using a Physical Electronics Model 5601 Microfocus ESCA System. Data collection and details of XPS spectral deconvolution (based on the method of target factor analysis, TFA) remain unchanged from that described previously [3]. Due to differences in corrosion oxide morphology between the present test and that encountered previously [3], further details are included here to illustrate the procedure used to convert sputter times into quantified (and verified) sputter depths.

In cases where the corrosion oxide exists as a true film, lacking in microscopic detail, sputter time can be converted into depth by multiplying by an experimentally-derived sputter rate. This result was readily determined by conducting periodic depth profiling experiments on an amorphous silicon dioxide (SiO_2) or tantalum pentoxide (Ta_2O_5) sputter standard having a known thickness. The thickness (1000 Å) was independently determined by profilometry. For general purpose work, the relative differences in sputtering rates between SiO_2 (or Ta_2O_5) and the transition metal oxides are estimated assuming that the sputter yield (i.e., atoms per argon ion) is independent of metal oxide. Since sputter rate is related to sputter yield by a specific grouping of physical properties: $\rho n/M$ (ρ is the oxide density, n is the number of atoms per molecule and M is the molecular weight) [11], sputtering rates relative to Ta_2O_5 are readily determined. On this basis, typical corrosion oxide spinels Fe_3O_4 (0.157 g-atoms cm^{-3}) and $FeCr_2O_4$ (0.155 g-atoms cm^{-3}) will sputter at rates within 20% of the rate for Ta_2O_5 (0.130 g-atoms cm^{-3}).

Stainless steel corrosion films differ from those formed on 'ideal oxide' sputter standards because they possess microscopic features that decrease sputter yield via surface roughening, crystal face orientation and shadowing effects. Therefore, sputter rates were determined by calibration using actual corrosion films whose thicknesses were independently measured. Oxide thicknesses were determined

independently by: (1) converting corrosion rates (determined by chemical descaling) into thickness using metal oxide density and (2) microscopically examining a cross-sectioned metallographic mount of the corrosion specimen. The two-step alkaline permanganate/ammonium citrate descaling method, which corrects for base metal attack, as described previously [3], was again used. Corrections for the small losses of oxide scale due to the corrosion release phenomenon were also accounted for by analyzing coupon weight changes prior to descaling. Due to the sub-micron oxide thicknesses expected, sufficient details from an edge-on cross-section were not obtainable at 10,000X magnification. Therefore, the cross-sectioning of a tungsten-coated metallographic mount was performed at an angle of 6° from the surface plane. This technique increased resolution by a factor of 9.6, i.e., $(\sin 6°)^{-1}$.

It is noted that previous applications of the above methodology found that the argon sputtering rate through corrosion films on iron-base CrNi alloys was equal to the Ta_2O_5 sputtering rate divided by a factor between 1.85 and 2.62; the calibration factor increasing with the size of the outer layer crystals [12, 3].

RESULTS

A. SEM

Appearances of the corroded 304 stainless steel specimens corresponding to exposure times between 1000 and 10,000 hours are shown in Fig 1 (10,000X). It is seen that the initial exposure period created a nearly complete surface covering by a base layer of submicron (<0.5 μm), polyhedral crystals. The crystal faces were oriented in such a manner which showed them to be protruding from a smooth substrate. Minor increases in crystal size, along with complete surface coverage and overlapping growth faces, were observed with increasing exposure time.

In situ measurements of oxide crystal composition by EDX proved inconclusive, due to the small crystal size and penetrating nature of the probe. To eliminate substrate interference, crystals from the outer layer were removed using replicating tape prior to performing EDX. Analyses of 10 randomly selected, <0.5 μm crystals from an 8000 hr specimen (S90) are summarized in Table I. Assuming a single phase spinel to be present indicates that the oxide crystals are predominantly ferrite (<5% chromite) having an average composition $(Ni_{0.1}Zn_{0.5}Fe_{0.4})Fe_2O_4$.

B. Grazing Incidence X-Ray Diffraction

A full scan GIXRD pattern of a 10,000 hr specimen (S70) is shown in Fig. 2 for ϕ (grazing incidence angle) = 0.5°. All peaks correspond to spinel plane reflections. No other crystalline phases, such as unoxidized 304 stainless steel substrate or ZnO, were detected.

The thickness of the spinel oxide corrosion layer was estimated by monitoring the emergence of the 304 stainless steel [111] XRD peak at several incident angles between ϕ = 0.3 and 0.7°. The [111] peak (at 2θ = 32.3°) was selected for analysis because it is the strongest peak and is readily distinguishable from the nearest spinel [400] peak at 2θ = 31.85°. As shown in Fig. 3, the [111] peak for 304 stainless steel first appeared at ϕ = 0.6°, providing an estimated oxide thickness of 0.22 μm using the expected relationship between ϕ and penetration depth.

Determination of unit cell dimensions of the spinel phase was not straightforward because of two complicating factors: (1) asymmetries were detected in all spinel peaks and (2) corrections to 2θ were necessary to account for the change in index of refraction between spinel and air when ϕ was less than

0.1 radian. The first required that the XRD spectrum be 'preprocessed' by fitting each peak to a sharp and broad component, see Fig. 4. Based on fitted half-widths (FWHM), wavelength of X-radiation ($\lambda = 1.15$ Å) and $\theta = 13°$, application of the Scherrer equation

$$size = \frac{0.94\lambda}{FWMH.\cos\theta}$$

indicates that the sharp peaks represent 700 Å (0.07μm) crystals, while the broader components may correspond to smaller crystals. Because the indicated size of the large(r) crystals agrees with the outer oxide ferrite crystals shown in Fig. 1, it is concluded that a direct correspondence exists between the two. Therefore, the fitted positions of these peaks in the spinel spectrum were subjected to further analysis.

Since the index of refraction of X-rays in the spinel oxide phase was slightly less than unity, all diffraction peaks were shifted to slightly higher angles than those calculated from Bragg's law. In conventional X-ray diffractometry the shift is usually neglected. However, for small incidence angles the Bragg angle shift due to refraction is much higher and must be taken into account when determining accurate lattice spacings. For $\phi < 0.01$ rad, Reference [13] provides the shift in 2θ as

$$\Delta 2\theta = 2\theta_{obs} - 2\theta_{cor}$$
$$= \frac{2\delta}{\sin(2\theta_{cor})} - \frac{\delta}{\phi}$$

where $\Delta 2\theta$ and ϕ are in radians. The results of these calculations for $\phi = 0.5°$ are given in TABLE II. These corrections lowered the measured 2θ angles by 0.059 to 0.061°. The unit cell dimensions were

finally determined from the corrected peak positions by least-squares refinement. The results are provided below in TABLE II.

The estimated lattice parameter is nearly identical to that of Fe_3O_4 (8.396 Å, PDF 19-629). Because the lattice parameters of $NiFe_2O_4$ (8.339 Å, PDF 10-325) and $ZnFe_2O_4$ (8.441 Å, PDF 22-1012) bracket that of Fe_3O_4,, it is expected that an Fe-Ni-Zn spinel containing nearly equal amounts of Ni(II) and Zn(II) would also have a lattice parameter identical to that of Fe_3O_4. Therefore, a composition estimate of the (ferrite-based) outer layer spinel based on the lattice parameter leads to an inconclusive result.

Presently, an explanation for the asymmetric shoulder on each spinel peak is lacking. It is noted that two spinel phases having the same composition, but different sizes, would result in spectra with symmetric broadening. If the compositions were different (i.e., different lattice parameters) then asymmetric broadening would be expected, but the amount of separation would be different for each reflection plane. Since the 2θ separation between sharp and broad peaks was independent of 2θ, it cannot be concluded that the broad shoulder represents a second spinel phase. An alternate interpretation, requiring different (or changed) distributions of Zn((II) and Fe(II) ion nearest-neighbors, may be hypothesized. Such behavior may occur with immiscibility in the Fe_3O_4-$ZnFe_2O_4$ spinel binary, a phenomenon to be discussed later.

C. Argon Ion Sputter Gun Calibration for Depth Profiling XPS Analyses

Two additional, independent estimates of corrosion oxide thickness were obtained by: (1) applying gravimetric analyses to quantitatively remove the corrosion oxide from corrosion coupons and (2) examining a cross-sectioned metallographic mount of a corrosion specimen. Table III summarizes the amounts of corrosion measured on the larger size coupons (0.4078 dm^2 per coupon) exposed

simultaneously with the smaller, polished specimens. A small correction was applied to account for the difference between the amount of metal oxidized (i.e., corroded) and the oxidized metal inventory in the adherent metal oxide corrosion layer (i.e., scale). This correction was determined by comparing the increase in specimen weight caused by testing with that expected for two limiting cases: complete retention and complete release of the corrosion scale. In the case of zero release

final wgt. = pre-test wgt. + oxygen in corr. oxide + zinc pickup

Since the metal oxides formed during the corrosion process are known to be spinels, AB_2O_4, whose overall composition is known from Table V to be $(Ni_{0.11}Zn_{0.24}Fe_{0.65})(Cr_{0.43}Fe_{0.57})_2O_4$, the expected oxygen and zinc contents are 27.7 wgt % and 6.8 wgt %, respectively. Thus, the zero release case may be rewritten as:

final wgt. = pre-test wgt. + 0.527 (metals oxidized)

In the case of complete release

final wgt. = pre-test wgt. – (metals oxidized)

By expressing the post-test – pre-test weight difference as a fraction of the maximum change between the zero and complete release limiting cases, i.e., 1.527 x metals oxidized, the fraction of corroded alloy released to the water was determined. The results of these calculations are summarized in the final columns of Table III. These calculations indicate that nearly 20% of the corroded metal was released to the water. Upon subtracting the indicated amounts of release from the metals oxidized, the surface density of corrosion oxide on the 10,000 hr coupon becomes 9.94 mg dm^{-2}. Assuming an oxide density of 5.2 g cm^{-3} provides an estimated oxide thickness, t = 0.19μm.

A second estimate of oxide thickness was obtained by examining a tungsten-coated, cross-sectioned metallographic mount of a 10,000 hr corrosion specimen (S66). The tungsten coating served to define

the outer oxide/water interface and to ensure its integrity during the sectioning process. As mentioned previously, a low angle cut relative to the surface plane (6°) provided an increase in resolution by nearly a factor of 10. The resulting color-coded elemental Auger intensity maps for Fe, Cr, Ni, O, Zn and W for one segment of the cross-sectioned corrosion film are shown in Fig. 5. On this basis it is found that t = 0.27 μm..

Averaging the GIXRD (0.22 μm), gravimetric (0.19 μm) and cross-sectioning (0.27 μm) results for the 10,000 hr specimens results in an estimated oxide thickness of 0.23 μm for the 10,000 hr test specimens. A calibration factor for the argon ion sputter gun was, therefore, defined to provide the XPS O(1s) depth on the 10,000 hr specimen as 0.23 μm. For the Table IV data, this factor was equivalent to the Ta_2O_5 thickness divided by 1.09. This factor, which is smaller than found previously [3, 12], is consistent with the presence of smaller-size oxide crystals ($\leq$0.5 μm).

Besides providing information on oxide thickness, the elemental intensity maps of the cross-sectioned metallographic mount revealed a number of compositional details: (1) both Cr and O maps clearly identified the alloy/inner oxide and inner oxide/outer oxide interfaces, (2) the Fe, O and W maps revealed the porous nature of the iron oxide-rich outer layer, and (3) the uniformity of Zn throughout the inner and outer layers is also revealed, although lower concentrations of Zn, Fe and O in the outer layer may be a consequence of signal 'dilution' by W. The Ni map deserves special mention since nickel composition throughout the outer and inner layer oxides is low and rather uniform except in the zone closest to the interface between the inner oxide and alloy substrate. Here nickel concentrations are greater than in the base alloy. This region also coincides with lower oxygen concentrations. The apparent presence of metallic nickel may be a consequence of zinc incorporation/substitution: the

Ni(II) cations in the inner layer chromite that are replaced by Zn(II) cations are unstable, undergo reduction and recrystallize as Ni(0).

D. X-Ray Photoelectron Spectroscopy with Argon Ion Milling

Typical elemental composition versus depth profiles are shown in Figs. 6a and b for specimens having exposure times of 5000 and 10,000 hr, respectively. As expected, the major elements detected were oxygen, iron, chromium, zinc and nickel. Significant levels of carbon were also found on the surfaces of all specimens. Because the initial ion milling operation reduced the carbon signals to trace levels, it was concluded that carbon was present as an adsorbed layer of hydrocarbon contamination, and was neglected when performing further analyses.

The presence of an outer layer corrosion oxide, i.e., the observed polyhedral crystals, growing on the specimen surfaces in Fig. 1, tended to manifest themselves by causing elongated 'tails' in the oxygen profiles, see Fig. 6. Therefore, estimates of oxide thickness were obtained from the inflection point in each oxygen, i.e. O(1s), profile: a maximum in the first derivative represents the depth at which ion milling of the oxide layer exposed metal substrate at the most rapid rate. These results are summarized in Table IV. For consistency with the expected corrosion kinetics, increases in oxide thickness were correlated with a parabolic growth rate expression:

$$O(1s) = k_p (t)^{1/2}$$

By least-squares analysis, it was found that $k_p = 19.8 \pm 8$ Å $hr^{-1/2}$, so that an oxide thickness of 0.20 ± 0.08 μm is predicted after an exposure period of 10,000 hr.

The above oxide thickness estimates were refined and speciated by TFA; speciated profiles for the 5000 and 10,000 hr specimens being shown in Figs. 7 and 8, respectively. To facilitate *oxide* comparisons, two plots were generated for each speciated composition profile: (a) a cross-hatched/solid split between oxidized metal and unoxidized metal, and (b) the indicated stoichiometry of the spinel oxide $(Ni_yZn_zFe_{1-y-z})(Fe_{2-x}Cr_x)O_4$. This information is summarized in a tabular manner and integrated numerically to quantify the overall amount and stoichiometry of the corrosion film, see Tables V and VI. Regression of these values provides a parabolic rate constant of 0.090 ± 0.034 mg (metals) dm^{-2} $hr^{-½}$.

The above results indicate that 304 stainless steel may have corroded selectively, with iron and nickel being protected at the expense of chromium. Composition of the corrosion oxide versus alloy substrate, by constituent, is: 66 vs. 72 (wgt % iron), 4 vs. 9 (wgt % nickel) and 30 vs. 19 (wgt % chromium). However, as will be discussed, a more likely interpretation is that corrosion occurred non-selectively, chromium was retained in the oxide (due to its lower solubility in aqueous solution [14]) and a portion of the oxidized iron was selectively released to the water. Oxidized nickel was both released and recrystallized to nickel metal.

DISCUSSION

The corrosion of 304 stainless steel in hydrogenated water at elevated temperature leads to the formation of a two-layered, corrosion oxide film [3]. The oxide is classified as a spinel: AB_2O_4, where A represents a divalent cation and B represents a trivalent cation. No other oxide phases were detected. In the outer layer, Fe(III) is the main B constituent, while both Cr(III) and Fe(III) are present in the inner layer. The existence of two spinel oxide layers is believed to be a manifestation of immiscibility in the Fe_3O_4-$FeCr_2O_4$ binary [3].

Zinc treatment leads to incorporation of Zn(II) cations into the growing spinel oxide, which alters the overall rate at which the corrosion film is created and the split that occurs between the inner and outer layer oxides. Specifically, zinc treatment nearly eliminated the outer layer spinel. Outer layer crystal sizes were much smaller than in the baseline test [3] and remained in the sub-micron range. The composition of these crystals suggests that Zn(II) replaced Fe(II) in the A-cation sites; the measured distribution being 70 mol % Zn, 20 mol % Fe and 10 mol % Ni. The B-cation sites remained populated mainly by Fe(III); EDX analyses of isolated, <0.5 μm crystals finding <5 mol % Cr(III). Thus, zinc treatment did not significantly alter the trivalent cation composition of the outer layer. Surface XPS analyses, which indicated higher Cr(III) levels, i.e., 25 mol %, are believed to be biased high, since the porous nature of the outer layer causes XPS to include chromium from the underlying Cr(III) ion-rich inner oxide layer. An increase in the unit cell dimension from 8.387 Å in the baseline test [3] to 8.396 Å (see Table II) is consistent with zinc(II) ion incorporation into the ferrite, vis-à-vis the chromite, although lattice parameters for the $(Zn_zFe_{1-z})Fe_2O_4$ binary are unavailable. In addition, the unexplained, asymmetric nature of X-ray reflections from the spinel planes suggest that additional work in this area may prove useful.

It is probable that spinel immiscibility also plays a role in determining acceptable Zn(II) ion concentration ranges in the ferrite-based outer layer. In this case, the magnetite-franklinite binary becomes the appropriate spinel system. Because magnetite is a predominately inverse spinel [15] and franklinite is a normal spinel [16], significant solution non-idealities are expected. Accurate mixing data are available only for temperatures ≥900°C [17, 18]. However, an estimate of the consolute temperature can be obtained by applying the spinel mixing model formulated by O'Neill and Navrotsky [19]:

$$\Delta G_m = Wn(1-n) + \Delta G_{m,D}$$

Here W is the regular solution parameter (=2800 J mol^{-1}), n is the mole fraction of zinc ferrite and $\Delta G_{m,D}$ is a free energy term dependent on changes in disorder, i.e., normal vs. inverse cation distribution. The latter term reduces to the ideal mixing formula when the two spinels being mixed have the same degree of disorder.

Fig. 9 shows the calculated free energies of mixing for the Fe_3O_4-$ZnFe_2O_4$ binary at four isotherms between 227 and 527°C. The occurrence of ex-solution (immiscibility) is indicated by the existence of a common tangent line connecting two different solid solution compositions (solvi). This condition is first observed in Fig. 9 at 427°C. At 260°C, the zinc-rich solvus has the approximate composition $(Fe_{0.4}Zn_{0.6})Fe_2O_4$, while the iron-rich solvus is nearly pure magnetite, i.e., contains ~5 mol % $ZnFe_2O_4$. This analysis implies that zinc treatment will create an outer layer oxide that contains a minimum zinc ferrite fraction around 60 mol % (provided that zinc concentrations in the water remain comparable to those of iron). Although our experimental results are consistent with the predicted minimum, a broader database is required to verify the hypothesized connection.

On the other hand, the size range of crystals in the non-porous, tightly-adherent inner layer remained about the same as in the baseline test (~0.01 μm). Iron replacement by zinc was also observed in A-cation sites of the inner layer spinel: the distribution being 20 mol % Zn, 70 mol % Fe and 10 mol % Ni. The Cr(III)-Fe(III) split in the B-cation sites, however, was approximately 60-40, nearly the same as in the baseline test.

Mainly because of decreased amounts of outer layer film relative to inner layer film, the integrated composition of the entire corrosion film was found to be 60.2 wgt % Fe, 27.1 wgt % Cr, 9.4 wgt % Zn, and 3.9 wgt % Ni. When zinc is excluded and the results are renormalized, the oxide is seen to be depleted in iron (66.0 wgt % in corrosion film vs. 72.4 wgt % in base metal), enriched in chromium (29.7 wgt % in corrosion film vs. 19.0 wgt % in base alloy) and depleted in nickel (4.3 wgt % in corrosion film vs. 8.6 wgt % in base alloy). This behavior is consistent with a non-selective corrosion mechanism during which iron and nickel are selectively released to the water by the corrosion release phenomenon. Oxidized nickel was also depleted by recrystallization to the metallic state. Assuming complete retention of oxidized chromium in the corrosion film, a material balance for iron in the Table V results indicates that 40% of the oxidized iron had been released to the water. Since iron represents 72% of the corroded metals, the XPS results are consistent with a corrosion release of 30%. This result is consistent with the result obtained by gravimetric analyses in Table III, i.e., 20%.

Zinc treatment was observed to significantly reduce the corrosion rate of 304 stainless steel; a comparison of the parabolic rate constants yielding $k_p = 0.243 \pm 0.078$ mg (metal) dm^{-2} $hr^{-1/2}$ (zinc test) vs. 1.16 ± 0.05 (baseline test [3]). Thus, the addition of 30 ppb soluble zinc(II) ions to hydrogenated, ammoniated water lowered the corrosion rate of 304 stainless steel by about 75%.

As discussed previously [3], a $FeCr_2O_4$-based constituent of the inner layer oxide is responsible for providing a barrier to the inward movement of oxygen, i.e., the rate-controlling step in the oxidation reaction. Zinc treatment 'works' because it substitutes for Fe(II), thereby increasing the thermodynamic stability of the inner oxide layer, which lowers the corrosion rate. The lower rate of oxidation nearly shuts down the outward, counter-diffusion of iron ions that have been recrystallizing to form the outer layer. Auger microprobing of a cross-section of the corrosion film found elevated

nickel levels at the alloy substrate/inner layer interface. This behavior indicates that Ni(II) ion replacement by Zn(II) also occurred and provided a path for recrystallization of Ni(II) back to elemental nickel.

If, as a first order approximation, the chromite-based inner layer spinel is treated as $FeCr_2O_4$, which becomes $(Zn_zFe_{1-z})Cr_2O_4$ when soluble Zn(II) ions are maintained in the aqueous phase, the zinc substitution reaction may be written

$$z\ Zn^{2+}(aq) + FeCr_2O_4(s) \rightleftharpoons z\ Fe^{2+}(aq) + (Zn_zFe_{1-z})Cr_2O_4(s)$$

Both stoichiometric end members in this binary system are normal spinels, so immiscibility is not expected. Furthermore, if the kinetics for the substitution reaction are assumed to be more rapid than those for the corrosion reaction, a thermodynamic analysis of the equilibrium constant for the substitution reaction indicates that a correlation will exist between the ratio of Fe(II) to Zn(II) ions in solution and composition of the chromite solid, z. Note that the absence of a zinc(II) ion concentration gradient across the inner oxide layer (see Figs. 7 and 8) lends support to the assumption that Zn(II) ion uptake is at equilibrium. Presently, soluble zinc [Zn_{tot}] and iron [Fe_{tot}] levels averaged 0.46 and 0.01 micromolal, respectively, and z = 0.2. These results provide a value for the modified liquid-solid distribution coefficient, [Zn_{tot}]/[Fe_{tot}] divided by z/(1-z), as 0.184. Predictions must be deferred since thermodynamic properties of $ZnCr_2O_4$ are not yet available and a consensus needs to be established regarding speciation of soluble Zn(II) ion hydroxocomplexes at elevated temperatures. However, the recognition that zinc accommodation in FeCrNi alloy corrosion films is concentration dependent (as implied by the above analysis) is consistent with the observed reductions in stainless steel corrosion

caused by increasing zinc levels [20]: 0.20 micromolal Zn decreased corrosion by 27%, while 0.80 micromolal Zn decreased corrosion by 96%, compared to a non-zinc baseline test in pure water.

ACKNOWLEDGEMENT

The professional assistance of the following individuals is gratefully acknowledged: Dr. Y. Gao (grazing incidence XRD, General Electric Co. CR&D Center), Dr. H. M. Tunison (chemical descale analysis), G. M. Neugebauer (SEM) and A. E. Ferguson (met mount).

REFERENCES

[1] B. Strauss, Proc. ASTM 24 (1924) 208

[2] L.W. Niedrach and W.H. Stoddard, Corrosion 42 (1986) 546

[3] S. E. Ziemniak and M. Hanson, Corros. Sci. (submitted)

[4] J. D. Dunitz and L. E. Orgel, J. Phys. Chem. Solids 3 (1957) 318

[5] A. Navrotsky and O. J. Kleppa, J. inorg. nucl. Chem. 29 (1969) 2701

[6] A. G. Crouch and J. Robertson, Acta metall. mater. 38 (1990) 2567

[7] S. E. Ziemniak, PPChem. 3 (2001) 193

[8] G. H. Vineyard, Phys. Rev. B26 (1982) 4146

[9] M. F. Toney, T. C. Huang, S. Brennan and Z. Rek, J. Mater. Res. 3 (1988) 351

[10] R. Jenkins and R. L. Snyder, Introduction to X-Ray Powder Diffractometry, John Wiley & Sons, New York, 1996

[11] M. P. Seah and C. P. Hunt, J. Appl. Phys. 56 (1984) 2106

[12] R. K. Wild, Surf. Interface Anal. 14 (1989) 239

[13] G. Lim, W. Parrish, C. Ortiz, M. Bellotto and M. Hart, J. Mater. Res. 2 (1987) 471

[14] S. E. Ziemniak, M. E. Jones and K. E. S. Combs, J. Solution Chem. 27 (1998) 33

[15] J. Nell, B. J. Wood and T. O. Mason, Amer. Mineral. 74 (1989) 339

[16] H. St. C. O'Neill, Eur. J. Mineral. 4 (1992) 571

[17] I. Katayama, J. Shibata, M. Aoki and Z. Kozuka, Trans. Jpn. Inst. Metals 18 (1977) 743

[18] I. Satoshi and A. Takeshi, Shigen, Sozai Gakkai Kenkyu, Gyoseki Happyo Koenkai Koen Yoshishu, (1990) 359

[19] H. St. C. O'Neill and A. Navrotsky, Amer. Mineral. 69 (1984) 733

[20] M. Haginuma, S. Ono, K. Takamori, K. Takeda, K. Tachibana and K. Ishigure, Zairyo to Kankyo 46 (1997) 565

TABLE I

Composition of Oxide Crystals in Surface Layer
Stripped from 8000 hr Exposure Corrosion Specimen (S90)

Particle No.	Metal Ion Content, Atom%			
	Fe	Cr	Ni	Zn
1	74.5	-	7.0	18.5
2	70.4	6.5	3.5	19.6
3	75.6	0.3	6.6	17.5
4	76.5	0.4	1.7	21.4
5	78.6	0.3	3.2	17.9
6	79.2	-	6.4	14.4
7	74.0	-	0.7	25.3
8	80.5	0.6	6.6	12.3
9	75.1	0.2	3.8	20.9
10	76.9	2.3	3.2	17.6
Avg.	76.1±2.8	1.1±1.9	4.3±2.1	18.5±3.4

TABLE II

Spinel Oxide Diffraction Peaks
Observed on 304 Stainless Steel Specimen (S70)
by Grazing Incidence X-Ray Diffraction ($\phi = 0.5°$)

Reflection Plane Indices, hkl	$2\theta_{obs}$	$2\theta_{cor}$
220	22.379	22.318
311	26.306	26.246
222	27.498	27.438
400	31.857	31.797
422	39.281	39.221
511	41.771	41.711
440	45.674	45.615
620	51.433	51.374
533	53.474	53.415
622	54.143	54.084
642	61.784	61.725
553	63.605	63.546
800	66.579	66.520
	Unit Cell Lattice Parameter, Å	8.3956(6)

TABLE III

304 Stainless Steel Corrosion and Release Estimates
Obtained by Gravimetric Analyses

Exposure hrs (ID)	Total Corrosion mg (metal) dm^{-2}	Avg	Weight Change During Test, mg dm^{-2}	Zero Release Wgt. Change, mg dm^{-2}	Corrosion Release, %	Avg
1000 (20)	12.48 ± 0.25		5.54	6.58	6	
1000 (22)	12.56 ± 0.27		6.25	6.62	2	4
1000 (24)	10.27 ± 0.39	11.77 ± 1.06	4.83	5.41	4	
2000 (14)	10.40 ± 0.29		4.34	5.48	7	
2000 (16)	12.24 ± 0.44		4.88	6.45	8	8
2000 (18)	12.31 ± 0.22	11.65 ± 0.91	4.93	6.48	8	
5000 (8)	13.09 ± 0.12		4.59	6.90	12	
5000 (10)	13.71 ± 0.64		4.39	7.22	14	14
5000 (12)	11.50 ± 0.22	12.77 ± 0.93	3.85	6.06	16	
5000 (32)	17.29 ± 0.42		-0.27	9.11	36	
5000 (34)	16.41 ± 0.66		-0.32	8.64	36	36
5000 (36)	20.92 ± 0.07	18.21 ± 0.45	-0.25	11.02	35	
8000 (26)	20.87 ± 0.78		2.72	11.00	26	
8000 (28)	24.69 ± 0.91		1.52	13.01	31	32
8000 (30)	25..36 ± 0.42	23.64 ± 0.73	-1.47	13.36	38	
10,000 (2)	11.18 ± 0.17		2.18	5.89	22	
10,000 (4)	12.75 ± 0.10		2.89	6.72	20	18
10,000 (6)	12.43 ± 0.69	12.12 ± 0.41	4.36	6.55	12	

TABLE IV

Surface Oxide Layer Thickness of Type 304 Stainless Steel
Based on Intensity of O(1s) XPS Peak

Exposure Time, hrs	O(ls) Depth, Å
1000	1597
2000	2405
5000	1897
5000	2134
8000	1575
10,000	2303

TABLE V

304 Stainless Steel Corrosion Film Characterization
by Integration of Speciated Composition Profile

Exposure Time, hrs	Metal Ion Content mg/dm^2	Distribution, wgt%			
		Fe	Cr	Ni	Zn
1000 (S86)	6.67	63.2	24.7	5.2	6.9
2000 (S82)	10.40	61.8	26.6	4.7	7.0
5000 (S74)	7.99	61.6	25.6	4.7	8.1
5000 (S96)	8.50	54.5	31.2	2.0	12.2
8000 (S92)	(5.67)	(36.8)	(47.2)	2.7	13.3
10,000 (S66)	8.86	59.7	27.4	3.8	9.0
	avg:	60.2±3.0	27.1±2.2	3.9±1.2	9.4±2.5
	avg (w/o Zn)	66.0	29.7	4.3	-
	304 SS assay, normalized	72.4	19.0	8.6	-

( ) deleted from average, suspect loss (sloughage) of outer layer crystals

TABLE VI

Spinel Composition $(Ni_yZn_zFe_{1-y-z})(Fe_{2-x}Cr_x)O_4$ of
Surface and Inner Corrosion Layers on 304 Stainless Steel

Exposure Time, hrs	Surface Layer			Inner Layer		
	y	z	x*	y	z	x
1000 (S86)	0.15	0.6	0.5	0.1	0.2	1.1
2000 (S82)	0.1	0.7	0.4	0.1	0.2	1.2
5000 (S74)	0.1	0.7	0.5	0.1	0.2	1.1
5000 (S96)	0.05	0.8	0.5	0.1	0.25	1.25
8000 (S92)	0.05	0.8	0.8	0.05	0.25	1.8
10,000 (S66)	0.1	0.8	0.4	0.1	0.2	1.2

avg: $(Ni_{0.1}Zn_{0.7}Fe_{0.2})(Fe_{0.75}Cr_{0.25})_2O_4$
$(Ni_{0.1}Zn_{0.2}Fe_{0.7})(Fe_{0.4}Cr_{0.6})_2O_4$

* Surface chromium XPS analysis may be biased high, see discussion in text.

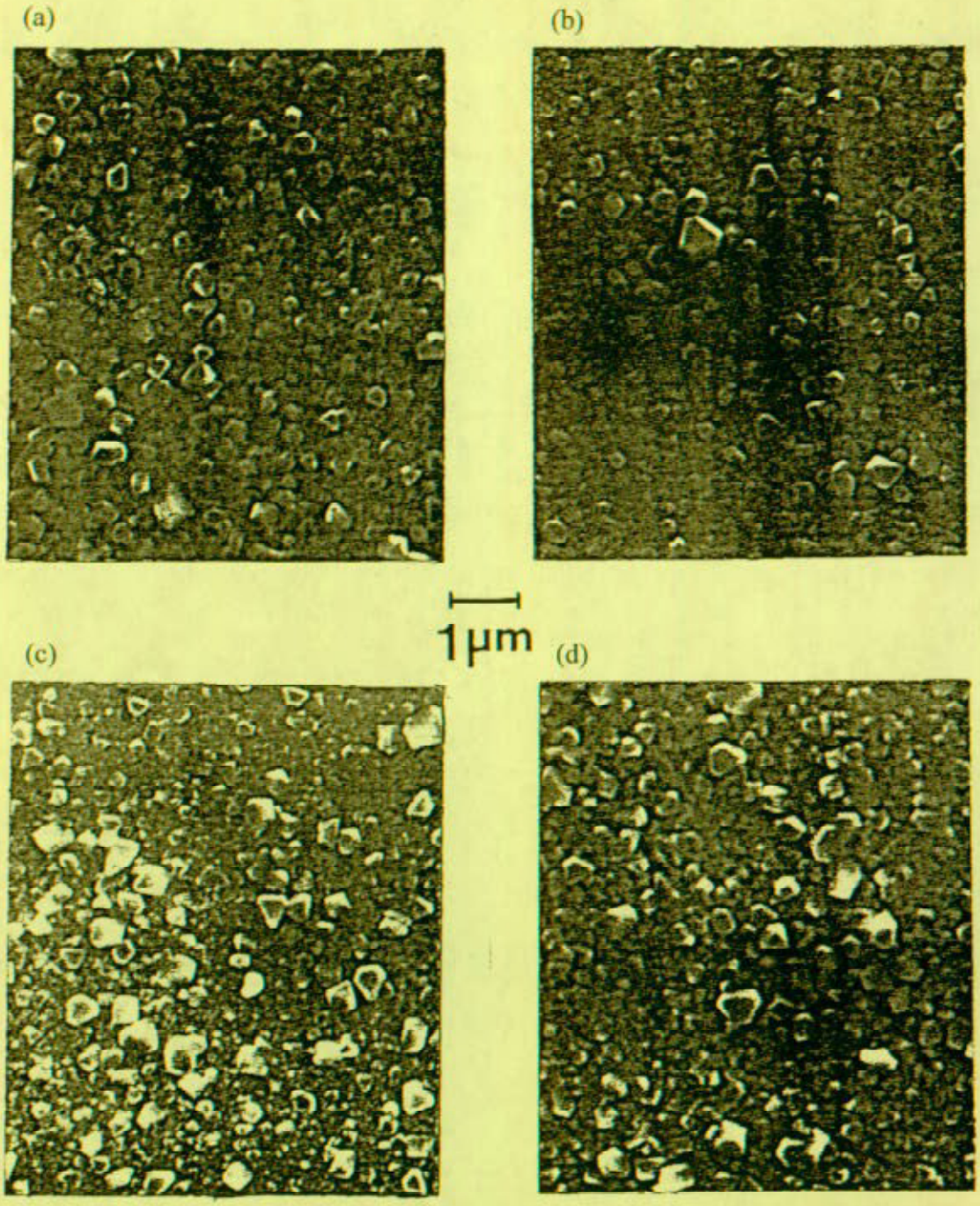

Fig. 1. High magnification SEM photographs of 304 stainless steel after exposure to zinc treatment: (a) 1000 hr, (b) 2000 hr, (c) 5000 hr and (d) 10,000 hr.

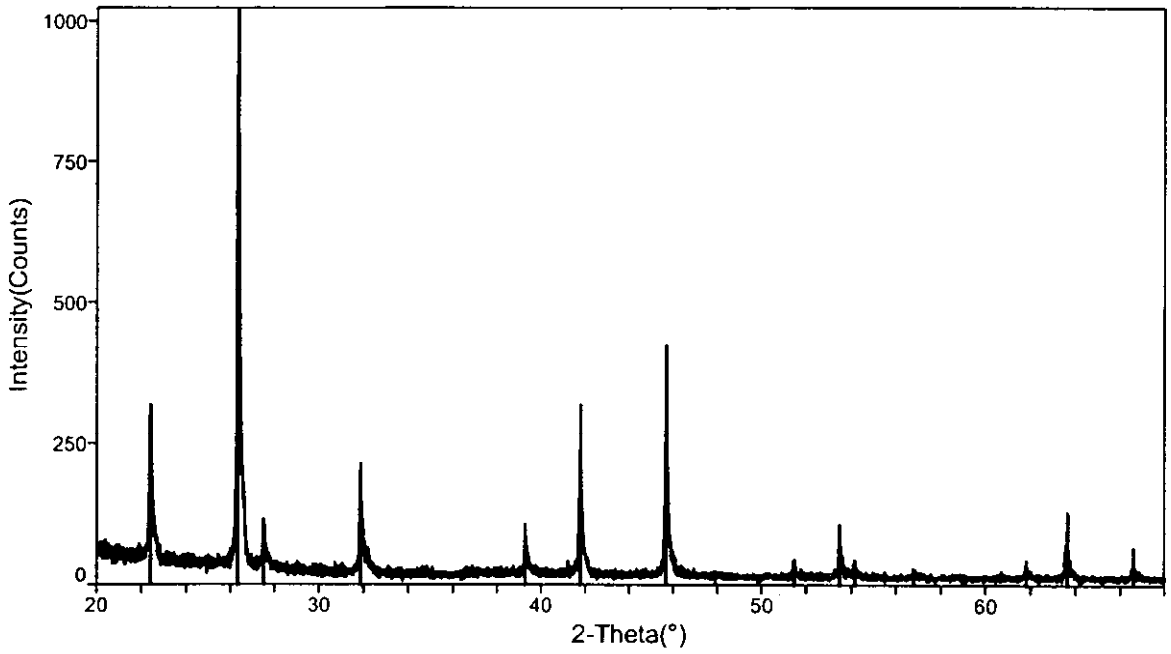

Fig. 2. Grazing incidence XRD scan ($\phi = 0.5°$) for 10,000 hr corrosion specimen (S70). All peaks can be identified as spinel phase, per comparison with PDF card 19-629 (Fe_3O_4).

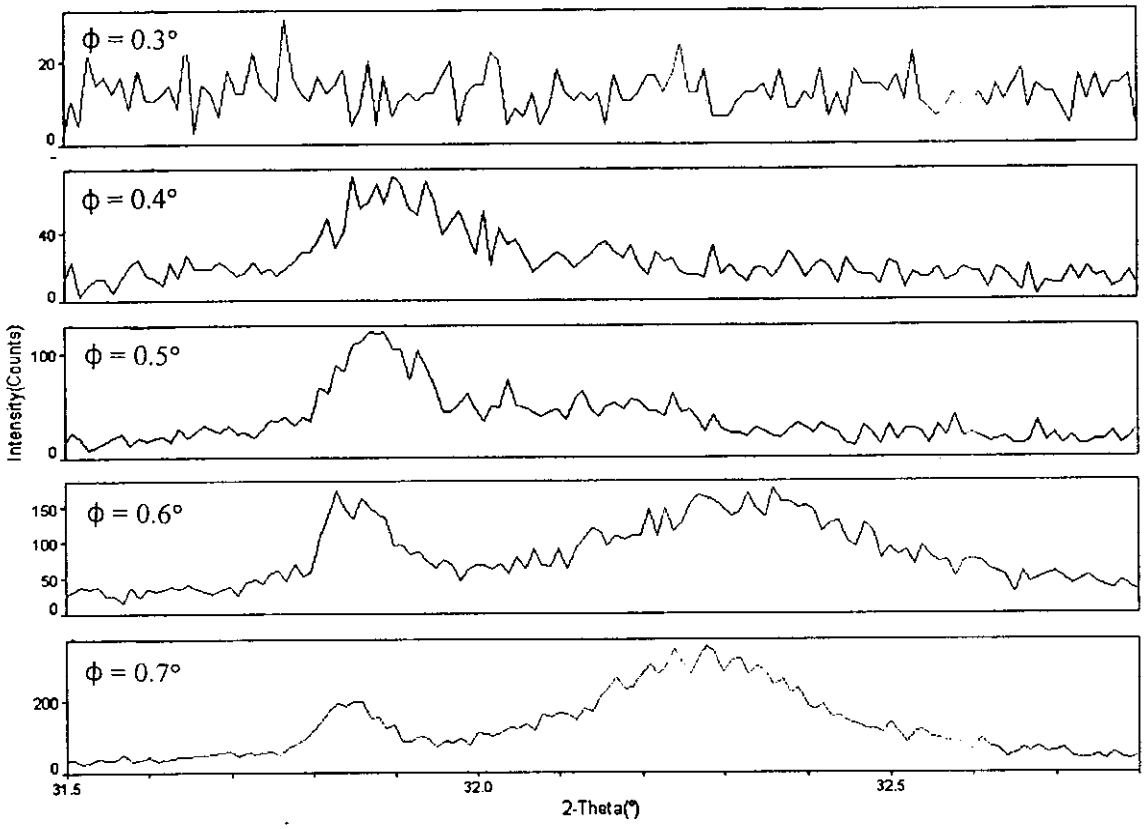

Fig. 3. Emergence of 304 stainless steel substrate [111] XRD peak in specimen S70 at incidence angles between 0.3 and 0.7°. Note appearance of substrate ($2\theta = 32.3°$) at $\phi = 0.6°$. The peak on the left at $2\theta = 31.85°$ represents the spinel [400] XRD peak.

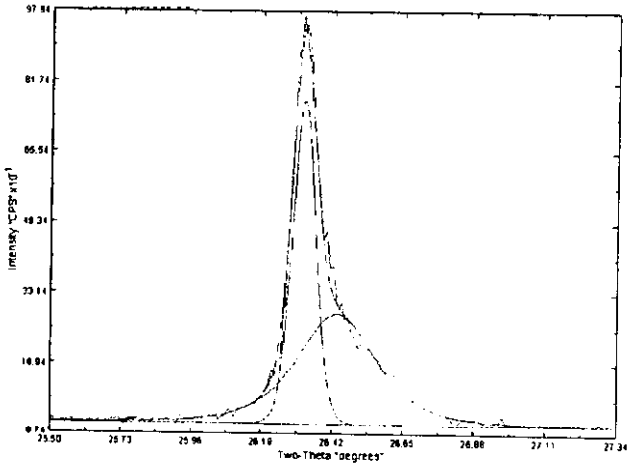

Fig. 4 High resolution plot of spinel [311] XRD peak at 2θ = 26.2° in Fig. 2 showing asymmetric broadening on higher 2θ side.

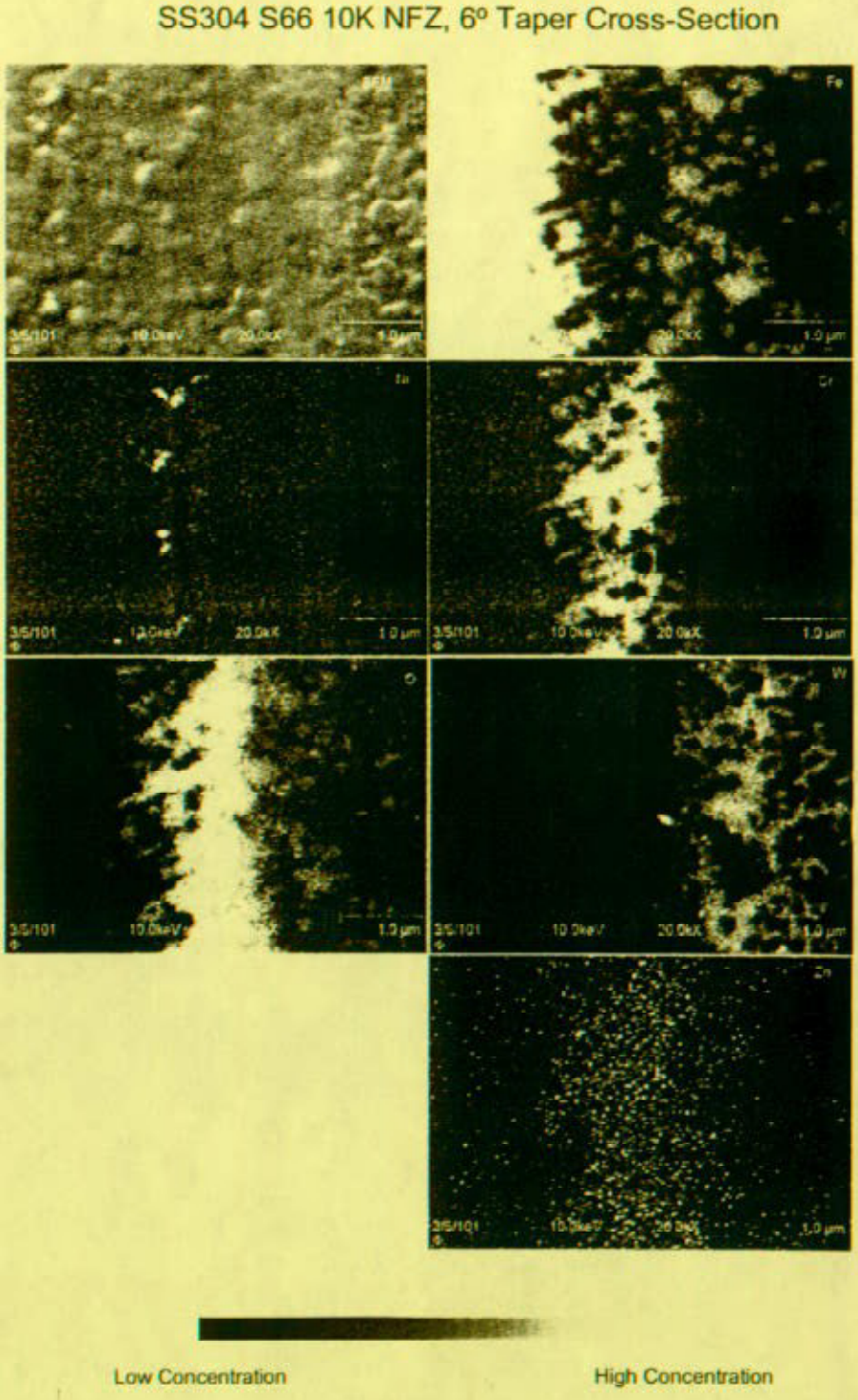

Fig. 5. Color-coded elemental Auger intensity maps of tapered cross-section of corrosion oxide on 10,000 hr specimen (S66): (a) oxygen, (b) iron, (c) nickel, (d) chromium, (e) zinc and (f) tungsten.

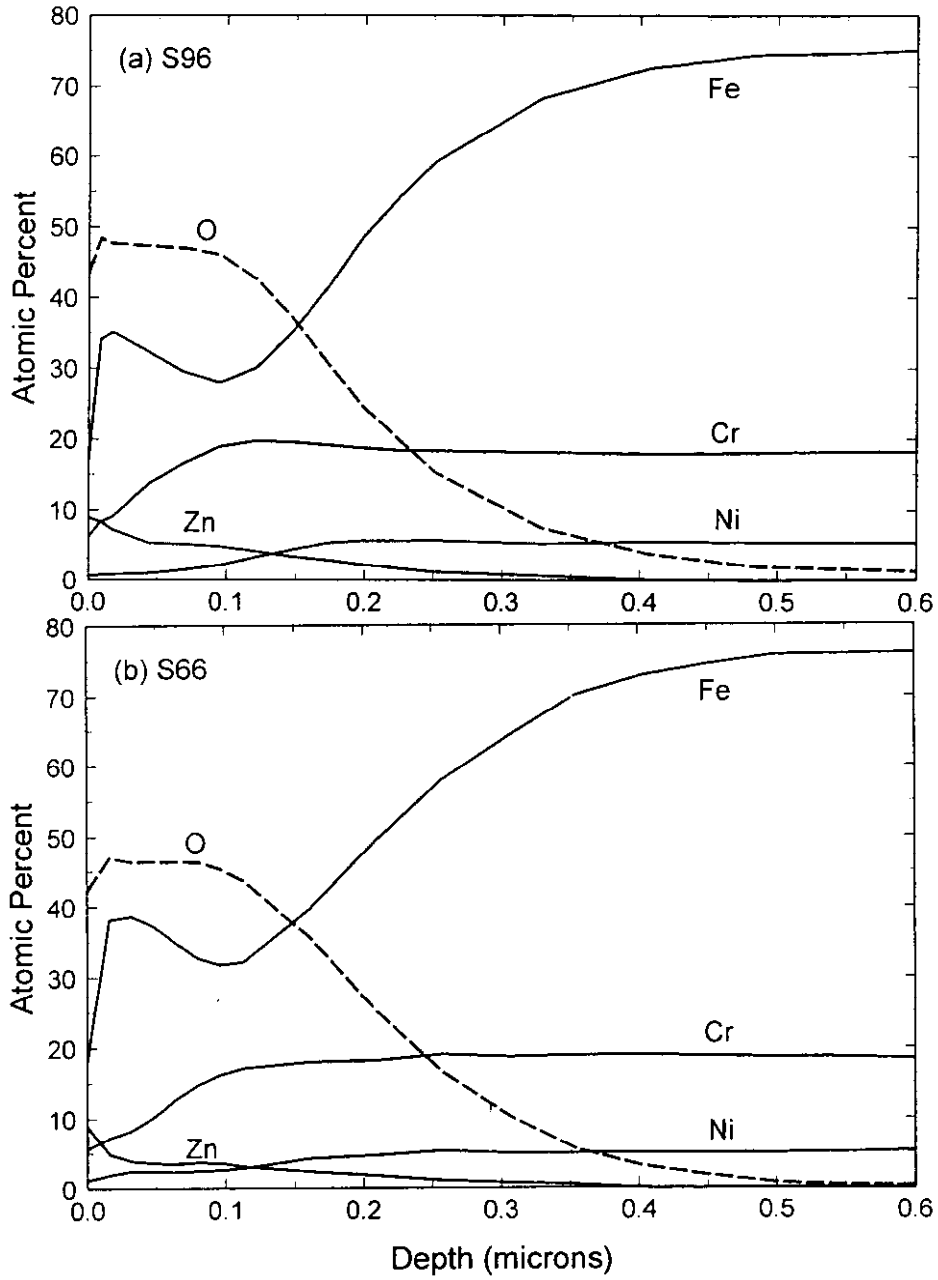

Fig. 6 Elemental composition versus depth profiles for 304 stainless steel specimens: (a) 5000 hr (S96) and (b) 10,000 hr (S66). Note elongated oxygen tails.

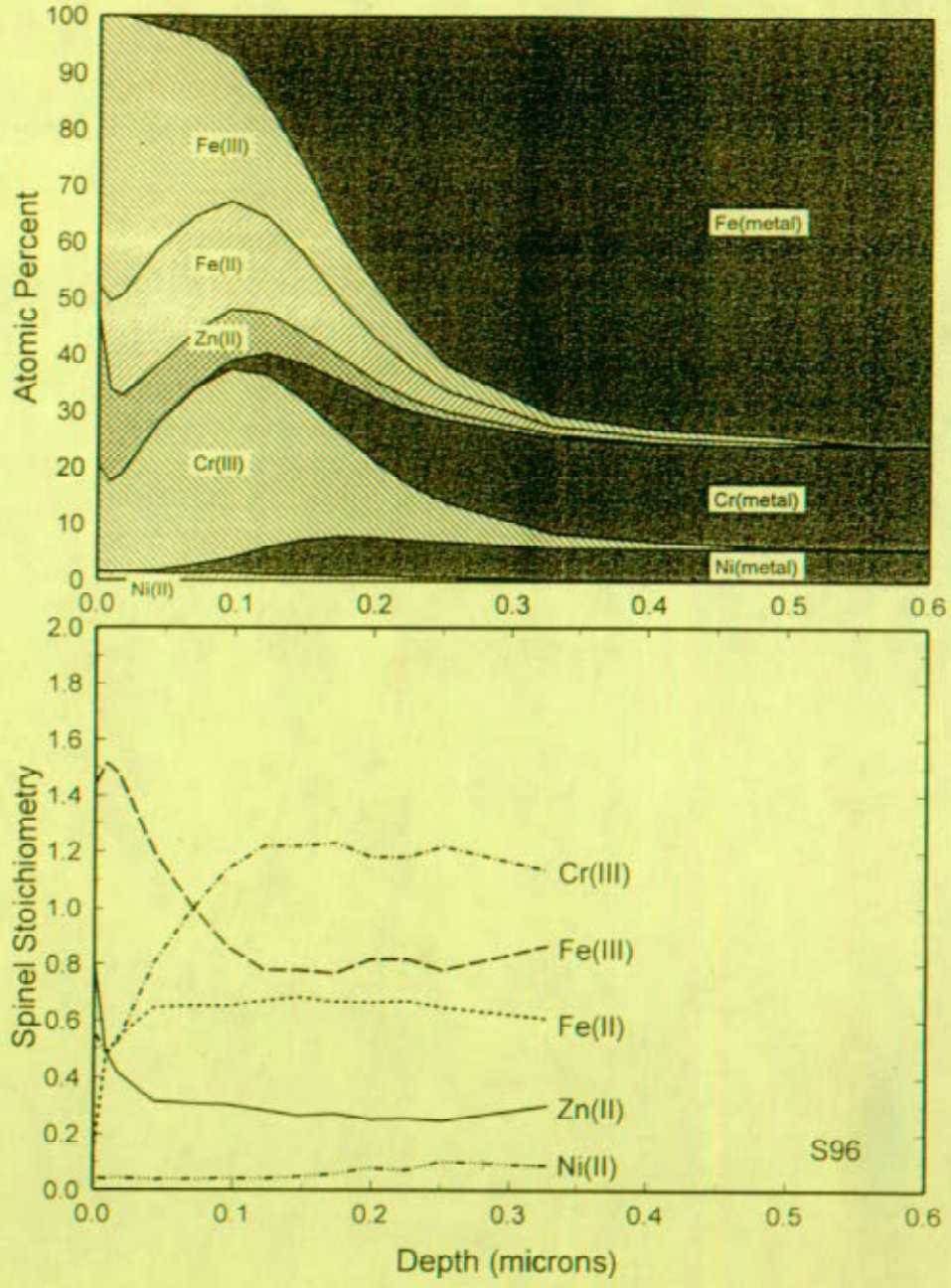

Fig. 7. Speciated composition profile of corroded 304 stainless steel surface after 5000 hr (S96).

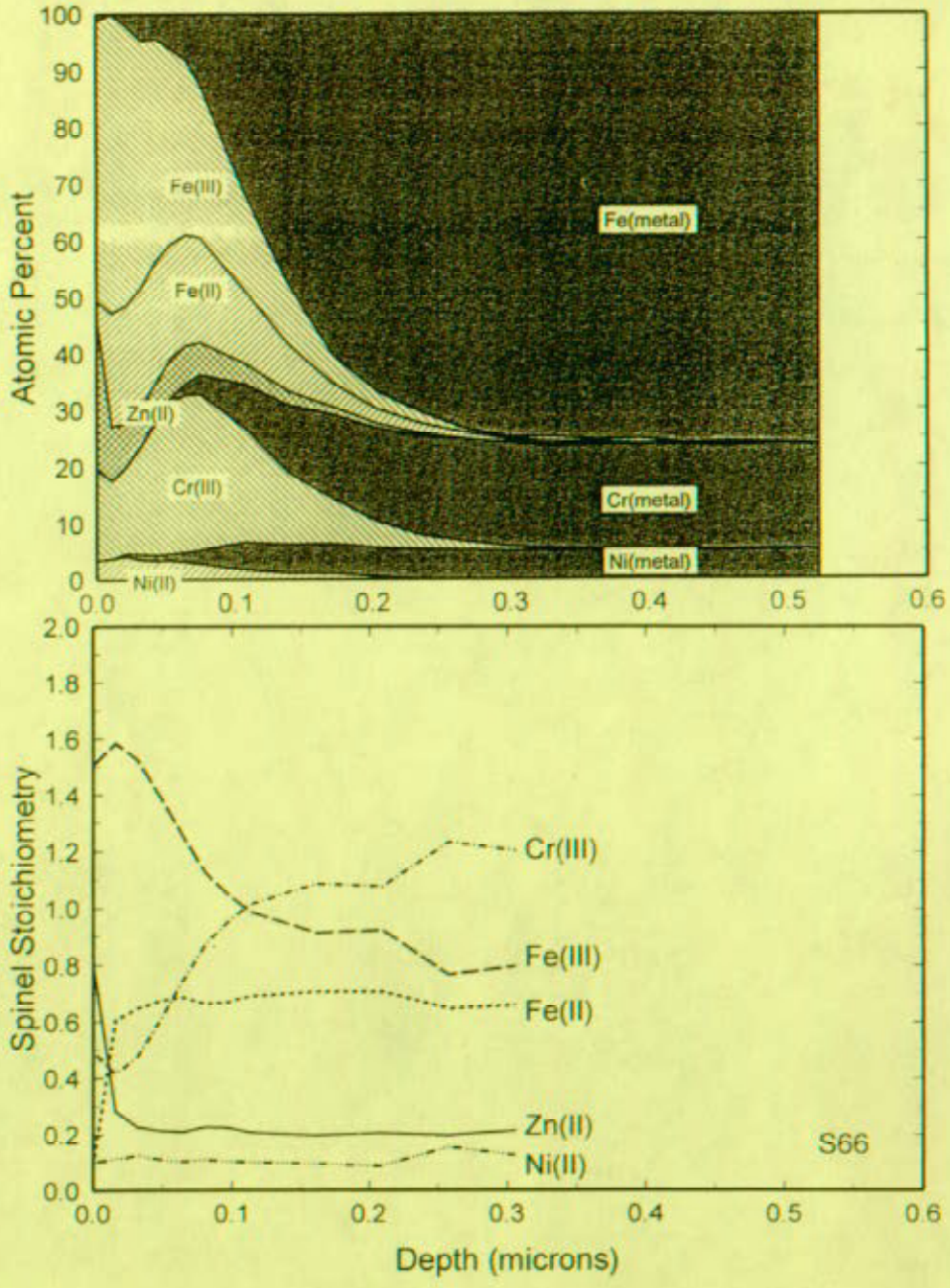

Fig. 8. Speciated composition profile of corroded 304 stainless steel surface after 10,000 hr (S66).

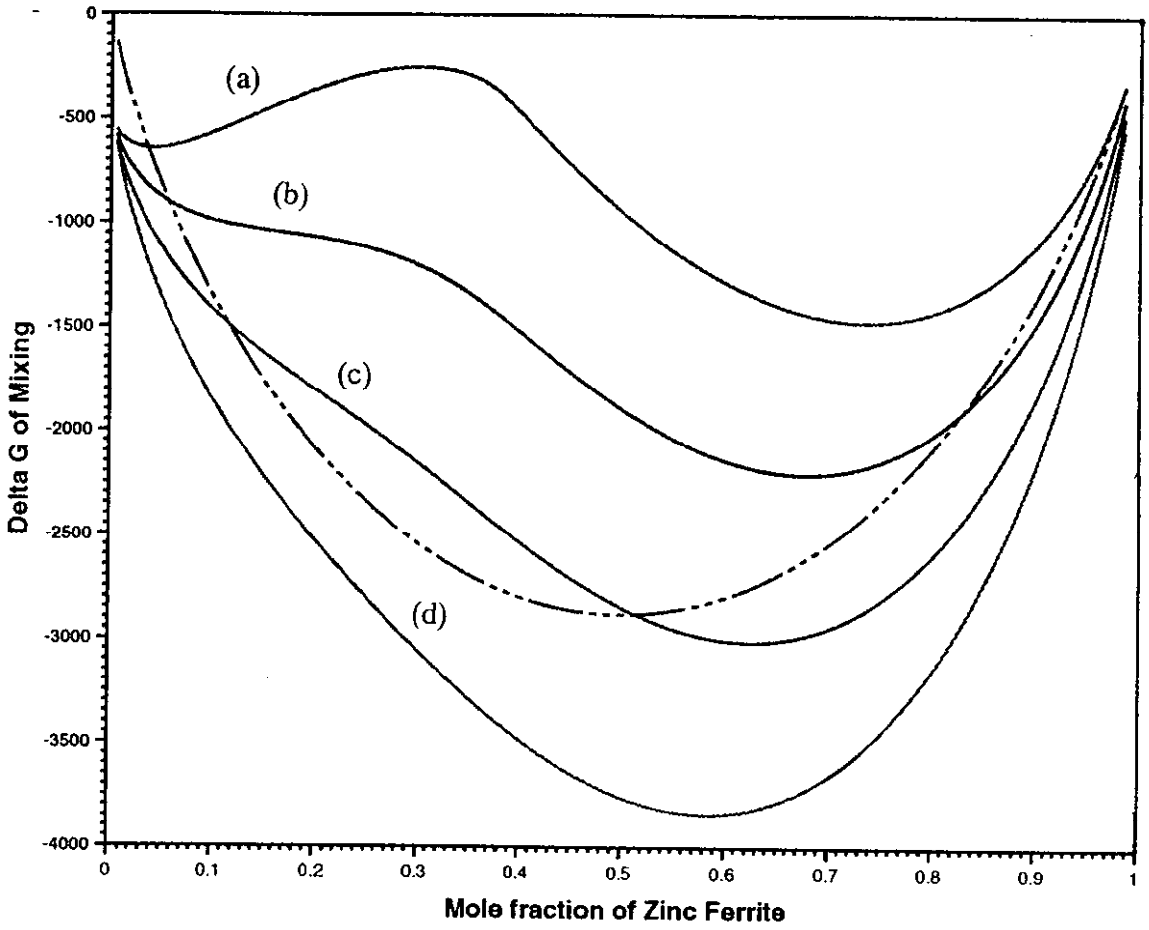

Fig. 9 Predicted free energies of mixing in the Fe_3O_4-$ZnFe_2O_4$ spinel binary at four temperatures: (a) 227°C, (b) 327°C, (c) 427°C and (d) 527°C. Dashed line represents ideal solution prediction at 227°C. Contribution from regular solution parameter is omitted for clarity.